WARWICK
THE UNIVERSITY OF WARWICK

Manuscript version: Author's Accepted Manuscript
The version presented in WRAP is the author's accepted manuscript and may differ from the published version or Version of Record.

Persistent WRAP URL:
http://wrap.warwick.ac.uk/181452

How to cite:
Please refer to published version for the most recent bibliographic citation information. If a published version is known of, the repository item page linked to above, will contain details on accessing it.

Copyright and reuse:
The Warwick Research Archive Portal (WRAP) makes this work by researchers of the University of Warwick available open access under the following conditions.

Copyright © and all moral rights to the version of the paper presented here belong to the individual author(s) and/or other copyright owners. To the extent reasonable and practicable the material made available in WRAP has been checked for eligibility before being made available.

Copies of full items can be used for personal research or study, educational, or not-for-profit purposes without prior permission or charge. Provided that the authors, title and full bibliographic details are credited, a hyperlink and/or URL is given for the original metadata page and the content is not changed in any way.

Publisher's statement:
Please refer to the repository item page, publisher's statement section, for further information.

For more information, please contact the WRAP Team at: wrap@warwick.ac.uk.

warwick.ac.uk/lib-publications

This article has been accepted for publication in IEEE Access. This is the author's version which has not been fully edited and content may change prior to final publication. Citation information: DOI 10.1109/ACCESS.2023.3337036

IEEE Access
Multidisciplinary | Rapid Review | Open Access Journal

Design and Investigation of a Metamorphic InAs Channel Inset InP HEMT for Cryogenic Low-Noise Amplifiers

SOUMAK NANDI[1], SHASHANK KUMAR DUBEY[2], MUKESH KUMAR[1], AMIT KRISHNA DWIVEDI[3], (Member, IEEE), MANISHA GUDURI[4], (Senior Member, IEEE) and AMINUL ISLAM[1], (Senior Member, IEEE)

[1]Department of ECE, Birla Institute of Technology Mesra, Ranchi-835215, India
[2]Department of ECE, G. Pullaiah College of Engineering and Technology, Kurnool, Andhra Pradesh, 518002, India
[3]School of Engineering, University of Warwick, Coventry CV4 7AL, United Kingdom
[4]School of Computing and Informatics, University of Louisiana at Lafayette, LA 70504, United States

Corresponding authors: Amit Krishna Dwivedi (e-mail: Amit.Dwivedi@warwick.ac.uk) and Shashank Kumar Dubey (dubey.shashank1991@gmail.com)

ABSTRACT This work proposes a 100 nm metamorphic InP HEMT with an InAs channel inset for cryogenic environment millimetre wave applications. The usage of an ultra-thin 2 nm barrier layer, unique composite channel topology and III-V material selection provides superior electron confinement in the channel, enhancing 2DEG concentration and mobility, thereby improving the speed of the proposed device. We achieve a unity current gain frequency (f_T) of 248.9 GHz and a maximum oscillation frequency (f_{MAX}) of 523.9 GHz with a current gain of 67.7 dB at 0.1 GHz, 298 K. A f_T/f_{MAX} of 5.02 GHz/10.01 GHz is achieved at 90 K. Off-state leakage current is in the nanoampere range with minimum noise figure (NF_{MIN}) of only 0.09 dB at 10 GHz, 90 K. We compare the DC, RF, noise and parasitic characteristics of the proposed device with other composite channel InP HEMTs proposed in latest works and showcase performance improvements in all domains. The performance achieved by using an InAs insert specifically is also justified, with InGaAs-InAs-InGaAs channel HEMTs providing 1.4 times better f_T and f_{MAX} with only half the NF_{MIN} of their InGaAs-InP-InGaAs channel counterparts. The proposed composite channel device showcases anomalous trends in electron scattering rate and electron mobility with impurity concentration and temperature variation. A novel frequency-and-temperature dependent small signal model has been put forth which accounts for these atypical cryogenic trends to accurately predict the behavior of the device under varying RF and temperature conditions.

INDEX TERMS Composite channel FETs, Cryogenic electronics, high electron mobility transistors (HEMTs), Low Noise Amplifiers (LNAs), Millimetre wave applications, Ultrathin Barrier

I. INTRODUCTION

Traditional silicon-based devices encounter performance limitations when operating in cryogenic environments, primarily due to heightened sensitivity to defects, impurity scattering, reduced carrier mobility, and thermal expansion mismatch [1]. To surmount the limitations faced by silicon devices at cryogenic temperatures, we use III-V materials which exhibit superior mobility and diminished impurity scattering, owing to lower extrinsic doping requirements [2]. The higher bandgap of III-V materials at the heterointerfaces enables superior electron confinement, enhancing carrier mobility. When designing a III-V heterostructure device, however, various III-V combinations can be considered for the formation of a HEMT [3], [4].

InP and GaAs have been selected for our proposed device due to their inherent material characteristics that facilitate optimal cryogenic performance. InP and GaAs possess relatively narrow bandgap energies of 1.35 eV and 1.42 eV respectively, in contrast to GaN's 3.39 eV bandgap [5]. This reduced bandgap allows for more accessible electron excitation at cryogenic temperatures, where thermal energy for electron excitation is substantially diminished [6]. Notably, InP exhibits relatively low thermal generation rates compared to other III-V materials, resulting in a significant decrease in the thermal generation of electron-hole pairs at cryogenic temperatures [7]. This characteristic contributes to maintaining lower noise levels and improving the overall signal-to-noise ratio in cryogenic devices [8]. Furthermore, InP exhibits excellent material stability under extreme low-temperature conditions, demonstrating minimal degradation in performance and reliability [9], [10]. For a typical FET device, the improvement of cutoff frequency and the reduction of noise

This work is licensed under a Creative Commons Attribution 4.0 License. For more information, see https://creativecommons.org/licenses/by/4.0/

This article has been accepted for publication in IEEE Access. This is the author's version which has not been fully edited and content may change prior to final publication. Citation information: DOI 10.1109/ACCESS.2023.3337036

and parasitics go hand in hand as given by the Fukui equation [11] (1), (2).

$$f_T = \frac{g_m}{2\pi} \frac{1}{(C_{GS}+C_{GD})(1+\frac{R_S+R_D}{R_{DS}})+g_m C_{GD}(R_S+R_D)} \quad (1)$$

$$NF_{MIN} = 10\,log(1 + 2\pi\, K_f\, f\, C_{GS}\sqrt{\frac{R_G+R_S}{g_m}}) \quad (2)$$

In composite channel FETs however, due to anomalous electron mobility and non-linear impact ionization behavior as proposed by Pozdnyakov's impurity dependent rate scattering and angle model [12] the Fukui model is inapplicable, particularly at cryogenic temperatures.

In composite channel HEMTs at cryogenic temperatures it is found that the HEMT layer topology that provides maximum cutoff frequency and the topology that provides minimized noise are different from one another, violating Fukui's model.

RF specialized InP HEMTs are being proposed to meet an acute industry demand for devices with high f_T, f_{MAX} and acceptable noise characteristics. 5G & 6G applications [13],[14], millimetre wave applications [15],[16], imaging applications [17], cryogenic applications [18]-[20], MMIC [21] and several emerging use cases [22] necessitate the usage of InP HEMTs for RF applications.

In this work, we design a composite channel HEMT and explain the tradeoff between gain optimization and noise optimization. The movement restriction and flow control of electrons within the composite channel are analyzed.

The bandgaps present on either side of the 2-dimensional-electron-gas (2DEG) and their effect on confining the majority charge carriers as they flow through the device is analyzed. The HEMT consequently proposed by utilizing our optimization supersede existing composite channel HEMTs in terms of RF, DC and noise characteristics. In Fig. 1, we compare our proposed HEMT with existing HEMTs [23]-[27] for LNA applications. Since f_T is proportional to L_G^{-2}, $f_T \cdot L_G^2$ is a constant for a given FET device [28]. Hence, comparing $f_T \cdot L_G^2$ allows one to compare the RF performance of FETs with different L_G values.

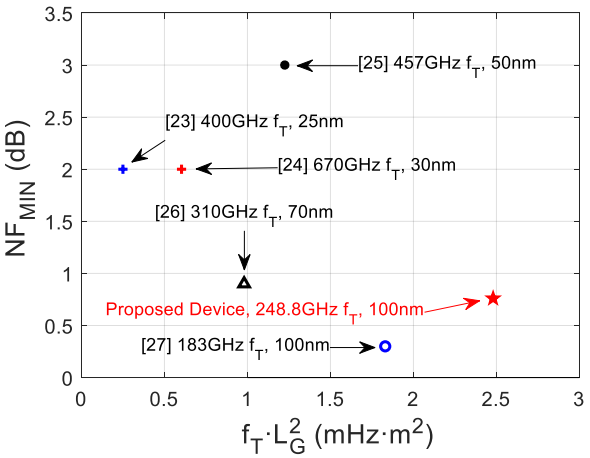

FIGURE 1. Comparison of simulation results of the proposed HEMT with measured data of recently suggested HEMTs for LNA applications.

II. DEVICE STRUCTURE AND SIMULATION ENVIRONMENT

The usage of a 2 nm ultrathin barrier layer and a channel inset in the proposed HEMT has been shown in the structure diagram Fig. 2. An $In_{0.08}Ga_{0.92}As$ passivation layer has been used to improve the noise performance of the device and an InP layer has been used as etch stop.

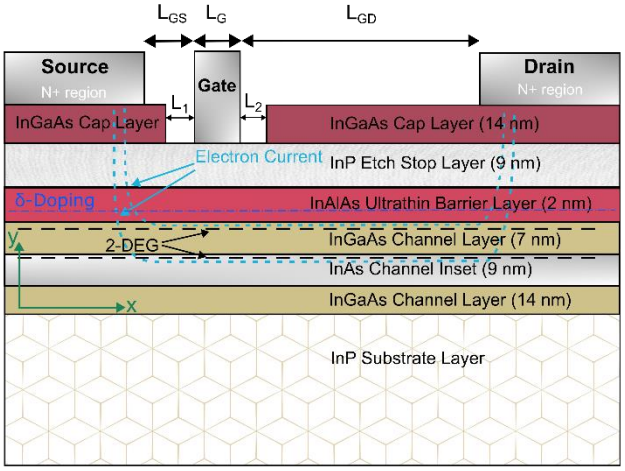

FIGURE 2. Structural diagram of the proposed HEMT.

TABLE 1. Optimized x-axis dimensions with 100 nm L_G.

Lateral Dimension	Optimized Value (nm)
L_{GS}	170 nm
L_G	100 nm
L_{GD}	530 nm
L_1	50 nm
L_2	50 nm

A. Ultra-thin barrier layer

When barrier thickness is reduced to the scale of the electron wavelength, quantum confinement effects dominate. Electrons in the 2-DEG are confined within the quantum well formed by the 2nm thin barrier layer and the heterojunction interface. Due to the reduced thickness, the quantum well potential energy profile becomes steeper, creating a stronger potential energy barrier, confining the electrons in the lateral direction to a narrow region near the heterojunction interface.

Electrons in the 2-DEG channel exhibit a wave-like nature and are subject to the principle of minimum energy. When the barrier layer is thin, the energy levels of the electrons become quantized within the quantum well. The electrons tend to occupy the lowest energy states available within the well, which correspond to the region near the heterojunction interface [29]. This energy minimization behavior further confines the electrons to a narrow region near the interface. Electrons on either side of the heterojunction occupy energy levels corresponding to an array of potential wells. Assuming the mass of an electron travelling within this array of potential wells to be m^*, in a well of width L_Z in the Z direction satisfies the free particle Schrodinger equation (3)

$$-\frac{h^2}{2m^*}\frac{d^2\psi}{dz^2} = E\psi \quad (3)$$

This work is licensed under a Creative Commons Attribution 4.0 License. For more information, see https://creativecommons.org/licenses/by/4.0/

This article has been accepted for publication in IEEE Access. This is the author's version which has not been fully edited and
content may change prior to final publication. Citation information: DOI 10.1109/ACCESS.2023.3337036

with eigenvalues (4),

$$E_n = \frac{\hbar}{2m^*}\left(\frac{n\pi}{L_z}\right)^2 = \left(\frac{\hbar^2\pi^2}{2m^*L_z}\right)n^2 \quad (4)$$

with eigenfunctions (5),

$$\psi_n = A\,sin(n\pi z/L_z) \quad (5)$$

where z is the perpendicular distance from the heterointerface, ψ denotes the amplitude of the charge carrier's wave motion, m^* denotes the mass of the charge carrier, L_Z is the width of the well within which electrons travel and n denotes the *nth* energy band from the heterointerface. The farther away an electron propagates from the heterointerface, the more excited it is (higher value of n in (4) and (5)). This causes it to vibrate away from well-defined planar wells in the 2DEG [30]. The movement of electrons perpendicular to the planar 2DEG region causes a loss in mobility within the 2DEG as the net velocity of the carriers is distributed across three dimensions instead of two [31]. If we create our material interfaces to be 1 nm – 2 nm in thickness, electrons are forced to occupy the low energy states near the heterojunction of the barrier-channel interface as higher energy states are physically absent. The effects of an ultrathin barrier layer help improve the electron current density of the upper 2DEG region from 1.94×10^8 A/cm^2 to 2.08×10^8 A/cm^2.

B. InAs Channel Inset

Due to the channel inset, two heterointerfaces are formed within the channel, resulting in two 2DEG (two-dimensional electron gas) regions. This is shown in Fig 3. where peak electron current density is observed in three regions- 3.96×10^8 A/cm^2 in the ultrathin barrier, 2.08×10^8 A/cm^2 in the upper InGaAs-InAs channel inset heterointerface and 1.94×10^8 A/cm^2 in the lower InAs-InGaAs channel inset heterointerface. This results in a "net" 2DEG electron current density of 4.02×10^8 A/cm^2 exceeding the 2.55×10^8 A/cm^2 electron current density observed in the single channel HEMT with the same dimensions. This results in improved f_T and f_{MAX} in the inset

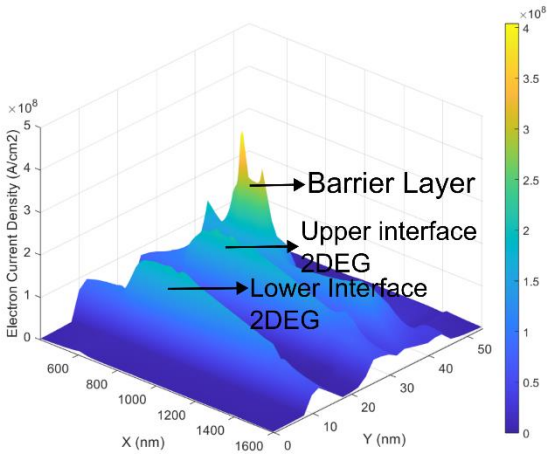

FIGURE 3. Electron current density within the device at the Barrier Layer and each of the two 2DEG regions.

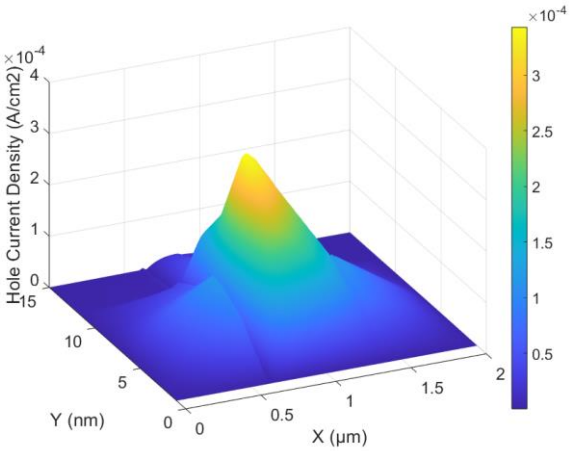

FIGURE 4. Peak hole current generation is observed underneath the gate at the second 2DEG region.

channel HEMT compared to the single-channel HEMT. Fig. 4 depicts the hole current generation in the device which was seen in the second 2DEG region alone.

C. Electrical and mathematical models

To accurately model charge carrier behavior, electron mobility at cryogenic temperatures was simulated using the Caughey-Thomas model while trap generation and recombination were simulated using the Shockley-Read-Hall model. The Caughey-Thomas mobility model is an empirical mobility model used for semiconductors. It was specifically used as it incorporates scattering mechanisms such as lattice scattering, impurity scattering, and surface scattering, all while being applicable at a wide temperature range (6) [32].

$$\mu_n(E) = \mu_{n0}\sqrt{\frac{1}{1+\left(\frac{\mu_{n0}E}{v_{sat}}\right)^2}} \quad (6)$$

where μ_{n0} is low-field electron mobility, E is the electric field, and v_{sat} is the electron saturation velocity. The electron saturation velocity is defined as 2×10^7 cm/s, which is obtained by linear interpolation from InAs and GaAs. Impact ionization and Band-Gap-Narrowing (BGN) models were used while employing Fermi-Dirac statistics instead of Boltzmann statistics due to the presence of high doping concentration.

D. Simulation Environment

1) Low Temperature Simulations

The intrinsic carrier concentration decreases with a decrease in temperature. In quasi-neutral regions, the minority carrier concentration can cause underflow. To avoid computational underflow in low temperature simulations, 160-bit precision computing is enabled in the ATLAS engine. Further, cryogenic material-specific models are enabled which help in achieving more accurate results at cryogenic temperatures.

This work is licensed under a Creative Commons Attribution 4.0 License. For more information, see https://creativecommons.org/licenses/by/4.0/

This article has been accepted for publication in IEEE Access. This is the author's version which has not been fully edited and content may change prior to final publication. Citation information: DOI 10.1109/ACCESS.2023.3337036

2) Impurity scattering

Lattice sites are several thousand times heavier than the charge carriers that travel through the device. Impurity scattering is consequently elastic in nature. For the energy distribution of simulated charge carriers to match the true charge carrier distribution, certain energy dissipation mechanisms are employed for carriers within the lattice. The Ridley impurity scattering model is implemented in the TCAD simulation. The scattering rate is calculated by the ATLAS engine upon enabling the RIDLEY flag.

Additionally, phonon scattering is computed by the ATLAS engine based on an energy dependent model stated as follows:

Deformation potential H' is computed as:

$$H' = E\frac{dy}{dr} \tag{7}$$

Where *dy/dr* is the deformation of the lattice due to phonons and E is the tensor that describes the shift in the electron band per unit deformation.

3) Lattice trap handling

Trap charges and corresponding trap carrier transitions that occur throughout the device were modelled using the Shockley-Read-Hall recombination model as shown in (8)

$$R_{SRH} = \frac{pn - {n_{ie}}^2}{TAUP0\left[n + n_{ie}\exp\left(\frac{ETRAP}{kT_L}\right)\right] + TAUN0n\left[p + n_{ie}\exp\left(\frac{ETRAP}{kT_L}\right)\right]} \tag{8}$$

Within this model, the ETRAP parameter handles trap charges and corresponding trap energy levels. Additionally, to enable electron trap modelling and hole trap modelling, DEVDEG.E and DEVDEG.H flags have been enabled in the Silvaco TCAD simulation tool.

4) Mobility modelling

To perform accurate low-field mobility modelling, the ANALYTIC and ARORA models are enabled. In this manner, when a lattice temperature is specified, temperature dependent parametric values are evaluated locally at each point in the device. When lattice heating is not enabled, the model employs a constant global temperature within the device. With lattice heating, the thermal generation caused by impurity scattering is accounted for by the simulator.

III. RESULTS AND DISCUSSION

A. DC performance

The I_{DS}-V_{GS} curve at 298 K is shown in Fig 5(a). The threshold voltage for which the device transitions from OFF to ON is negative, making it a depletion type device. The variation in these characteristics with a decrease in temperature is due to reduced thermal noise, which lowers the lattice scattering resulting in improved carrier transport efficiency. These trends are apparent in Figs. 5(b) and 5(c). Fig. 5(d) shows that the value of saturation-drain current reduces with temperature. I_{DS} values at 300 K and 100 K are compared for the same biasing.

For low electric fields in the barrier, gate leakage is dominated by trap-assisted tunneling (TAT) and Poole-Frenkel (PF) emission. Donor-like traps concurrently exist on the HEMT surface and the 2-DEG in the channel originates from the ionization of the donor-like traps. The leakage current density from the channel to the gate is modelled as trap-assisted tunneling current and has a similar form to that of thermionic emission (9) [33].

$$J_{TAT} = J_0\{exp[\frac{q(V_{GS}-V_0)}{\eta kT}] - 1\} \tag{9}$$

where, J_0, V_0, and η are parameters used to fit the experimental data, q is the fundamental electronic charge, k is the Boltzmann constant, and T is temperature. Poole-Frenkel emission describes emission from traps by thermal activation but with a lowered trap depth induced by Coulomb interaction. The leakage current density due to this effect is termed Poole-Frenkel leakage and can be expressed as [33]:

$$J_{PF} = C_{PF}\,E exp[-\frac{q(\phi t - \sqrt{qE/\pi\varepsilon_0\varepsilon_S}}{kT}] \tag{10}$$

where C_{PF} is a constant, E is the electric field across the barrier, ϕ_t is the barrier height for the electron emission from the trap state, ε_0 is the permittivity of vacuum, and ε_S is the relative permittivity of AlGaN at high frequencies. For high barrier electric field, Fowler–Nordheim tunneling dominates leakage effects. At higher electric fields, electrons in the gate may tunnel through a rounded triangular barrier. Such leakage is modelled as Fowler–Nordheim tunneling current density (11) [33].

$$J_{FN} = AE^2\,exp(-\frac{8\pi\sqrt{2m_e(q\phi_b)^3}}{3qhE}) \tag{11}$$

where ϕ_b is the Schottky barrier height. The net gate leakage current that is valid for a range of barrier electric fields can be expressed as (12).

$$J_G = J_{TAT} + J_{PF} + J_{FN} \tag{12}$$

The total gate leakage current in the 90 K – 150 K temperature range for the proposed device is shown in Fig. 5(e). The leakage current is observed to be in the sub-nanoampere range. A transient analysis of the proposed device was performed and is shown in Fig. 5(f). A minimum rise time and fall time of 3.1 ps was achieved corresponding to a driver switching time of 3 ps.

B. AC and Noise performance

As the operating frequency of the proposed HEMT is increased, several changes occur in transit time, parasitics and impedances within the device which manifest as a reduction in gain with an increase in frequency. As operating frequency increases, the time available for the carriers to travel through the device from the source to the drain decreases. This results in reduced gain as the carriers have less time to contribute to the output current. Parasitic capacitances associated with various device regions and

This work is licensed under a Creative Commons Attribution 4.0 License. For more information, see https://creativecommons.org/licenses/by/4.0/

This article has been accepted for publication in IEEE Access. This is the author's version which has not been fully edited and
content may change prior to final publication. Citation information: DOI 10.1109/ACCESS.2023.3337036

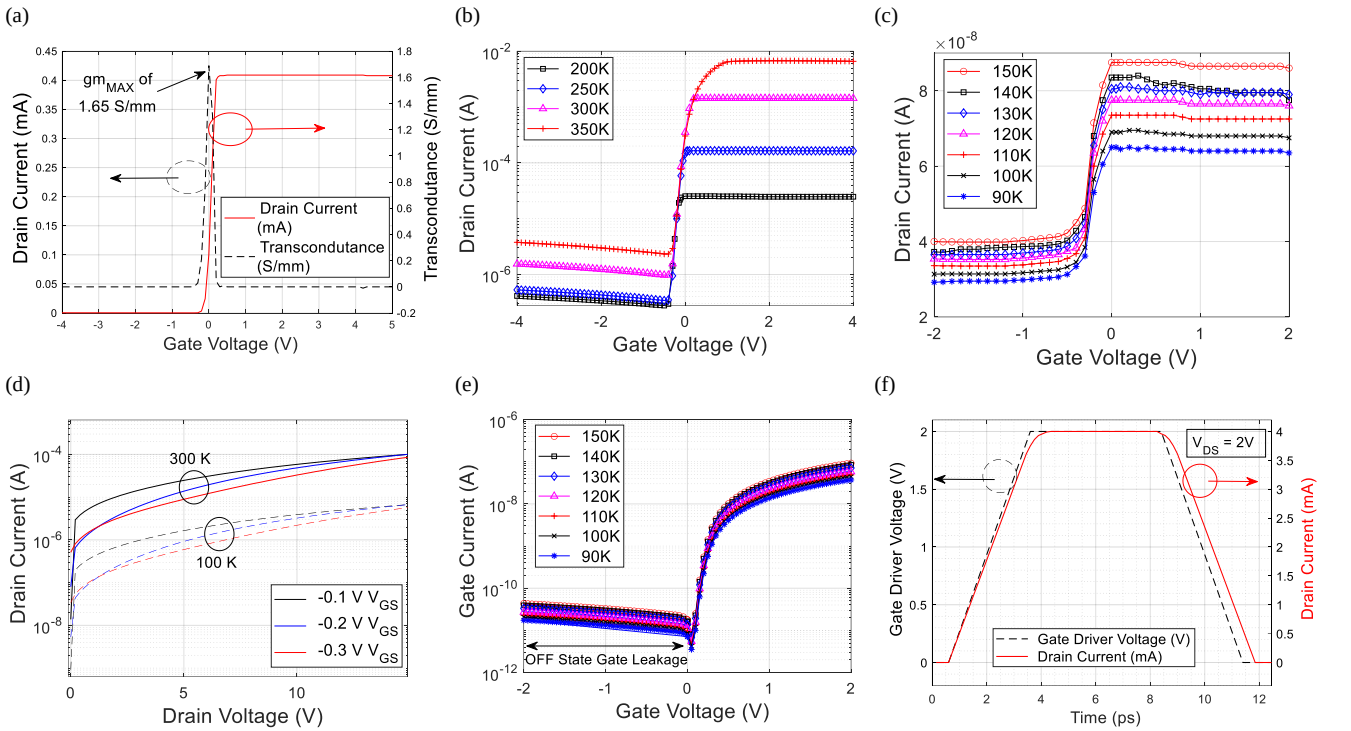

FIGURE 5. (a) . I_{DS}-V_{GS} of proposed HEMT at 298 K. Peak transconductance gm_{MAX} of 1.65 S/mm is observed. The solid curve shows the drain current in mA and corresponds to the left y-axis. The dashed curve shows transconductance in S/mm and corresponds to the right y-axis. (b) I_{DS}-V_{DS} curve of proposed HEMT in 350 K-200 K range for a device width of 500 µm. (c) I_{DS}-V_{GS} curve of proposed HEMT in 150K-90K range. (d) I_{DS}-V_{DS} curve of proposed HEMT at 300 K and 100 K. Black, blue and red lines denote V_{GS} biasing of −0.1V, −0.2V, −0.3V, respectively. Solid lines indicate behavior at 300 K and dashed lines indicate behavior at 100 K (e) Gate leakage characteristics: I_{GS}-V_{GS} curve of proposed HEMT in 150 K-90 K range. (f) Transient Analysis of the proposed HEMT. A minimum rise time and fall time of 3.1 ps was achieved corresponding to a driver switching time of 3 ps. The dashed curve shows gate driver voltage in V and corresponds to the left y-axis. The solid curve shows drain current in mA and corresponds to the right y-axis.

interconnects become more significant at higher frequencies.

The parasitic capacitances act as low-pass filters, attenuating the high-frequency components of the input signal. The roll-off of gain at 20 dB/dec rate is seen in our device across a range of temperatures seen in Figs. 6(a) to 6(d).

It is seen that f_{MAX} has a larger dependency on parasitic components than f_T. As parasitic components vary with temperature, f_{MAX} shows a larger temperature dependency than f_T, as is shown by the data in Table 2.

TABLE 2. Variation and f_T and f_{MAX} of the proposed HEMT with temperature

Temperature (K)	f_T (GHz)	f_{MAX} (GHz)
350	248.3	665.3
300	247.2	526.0
250	231.5	365.1
200	196.0	214.4
150	168	152
140	150	134
130	116	103
120	72.7	67.7
110	30.1	29.7
100	10.00	19.98
90	5.02	10.01

Noise must be reduced in an LNA to preserve the integrity of weak signals. By minimizing unwanted noise contributions, the LNA can enhance the signal-to-noise ratio, enabling accurate and reliable amplification of low-level signals without distortion or degradation.

The variation of NF_{MIN} (minimum noise figure) and G_N (noise conductance) in the cryogenic (90 K – 150 K) temperature range is shown in Fig. 6(e) and Fig. 6(g). The variation of NF_{MIN} and G_N in the 200 K – 350 K temperature range is shown in Fig. 6(f) and Fig. 6(h). T_{min} (minimum noise temperature) of the proposed HEMT in the cryogenic operation range has been computed using the Pospieszalski Noise Model [34]. The Pospieszalski Noise Model equation is given in (13).

$$T_{min} = \frac{f}{f_T}\sqrt{r_{gs}g_{ds}T_gT_d + (\frac{f_T}{f})^2 r_{gs}{}^2 g_{ds}{}^2 T_d{}^2} + 2(\frac{f_T}{f})r_{gs}g_{ds}T_d \quad (13)$$

where, r_{gs}, g_{gs}, T_g and T_d are small signal model parameters that are explained in section IV. The computed T_{min} lies between 6 K and 10 K at an ambient temperature of 90 K-110 K as shown in Fig. 6(i).

C. Material Selection for Channel Inset

Device performance using different composite channel materials has been analyzed. Using an InGaAs-InAs-InGaAs composite channel provided higher f_T and f_{MAX} than a full InGaAs channel as seen in Fig. 7(a) but displayed

This work is licensed under a Creative Commons Attribution 4.0 License. For more information, see https://creativecommons.org/licenses/by/4.0/

This article has been accepted for publication in IEEE Access. This is the author's version which has not been fully edited and content may change prior to final publication. Citation information: DOI 10.1109/ACCESS.2023.3337036

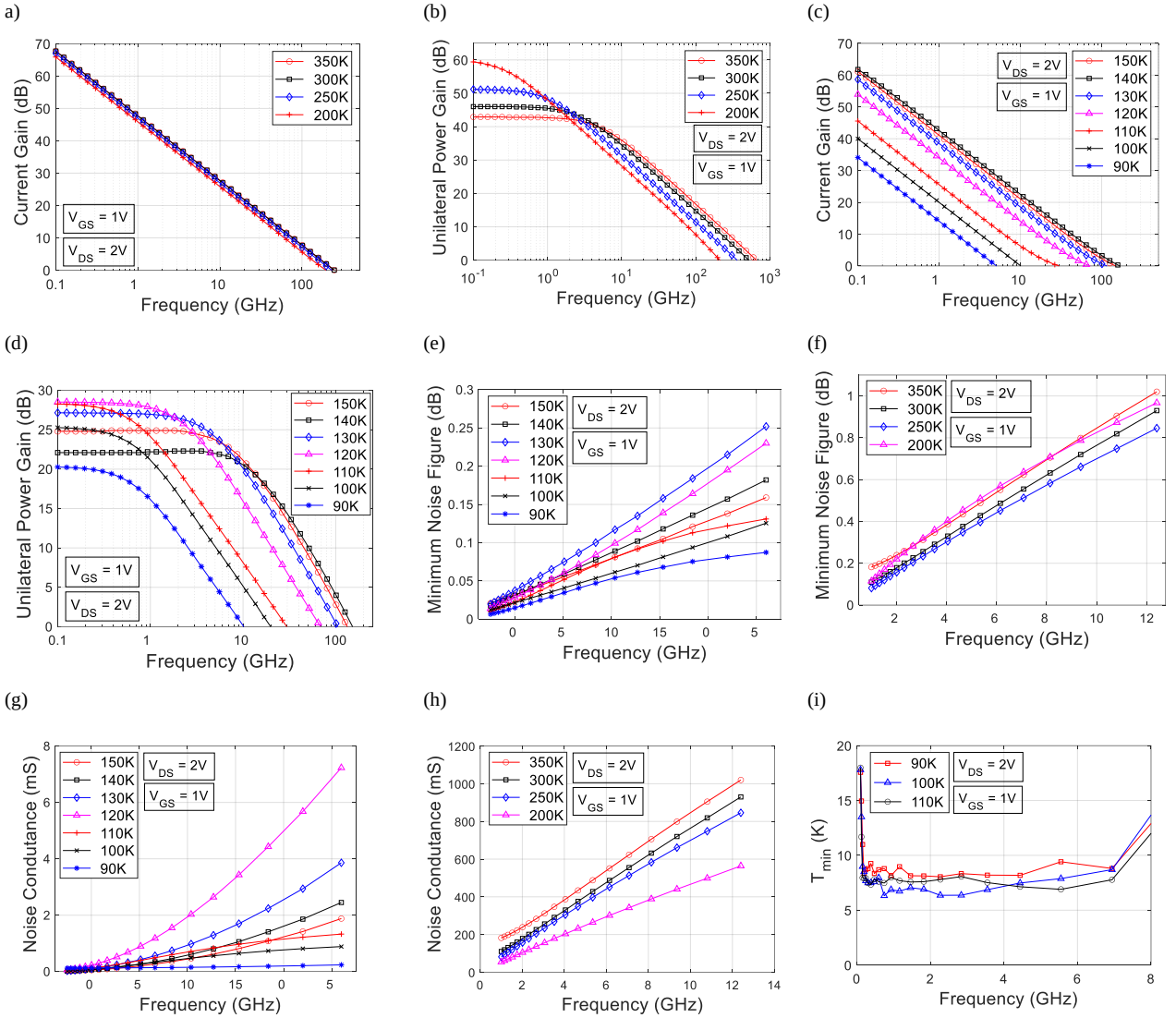

FIGURE 6. (a) Current Gain vs Frequency curve of proposed HEMT in 350 K-200 K range. (b) Unilateral Power Gain vs Frequency curve of proposed HEMT in 350 K-200 K range. (c) Current Gain vs Frequency curve of proposed HEMT in 150 K-90 K range. (d) Unilateral Power Gain vs Frequency curve of proposed HEMT in 150 K-90 K range. (e) Minimum Noise Figure vs Frequency curve of proposed HEMT in 150 K-90 K range. (f) Minimum Noise Figure vs Frequency curve of proposed HEMT in 350 K-200 K range. (g) Noise Conductance vs Frequency curve of proposed HEMT in 150 K-90 K range. (h) Noise Conductance vs Frequency curve of proposed HEMT in 350 K-200 K range. (i) Minimum Noise Temperature vs Frequency curve of proposed HEMT in 110 K-90 K range.

marginally higher NF_{MIN} as well due to the increased number of heterointerfaces in a composite channel.This is observed in Fig. 7(b). An InGaAs-InP-InGaAs composite channel, however, showed much worse performance than the InGaAs-InAs-InGaAs composite channel and full InGaAs channel, showcasing lower f_T and f_{MAX} and about twice the NF_{MIN} of the other two channel types as tabulated in Table 3.

The InGaAs-InAs-InGaAs composite channel structure, with its varying bandgaps, offers a higher cut-off frequency (f_T) and maximum oscillation frequency (f_{MAX}) due to improved electron confinement and transport. However, the presence of heterojunction interfaces and interface imperfections in the composite channel can introduce additional noise sources, affecting noise parameters such as NF_{MIN} and G_N (noise conductance).

Table 3. Variation of f_T, f_{MAX} and NF_{MIN} with channel composition.

Channel composition	f_T (GHz)	f_{MAX} (GHz)	NF_{MIN} at 10 GHz (dB)
InGaAs-InAs-InGaAs	248.9	523.9	0.764
InGaAs-InP-InGaAs	181.8	202.6	1.584
InGaAs	241.5	449.4	0.725

D. Non-linear parameter variation and optimization challenges

For inset channel devices, it is found that f_T, f_{MAX}, noise and other parameters do not vary predictably with variation in doping concentration. This is due to anomalous noise behavior attributed to impurity deionization. Noise often increases due to increased impurity concentration, and several works have been devoted to the investigation of electron scattering by impurity ions in semiconductors.

This work is licensed under a Creative Commons Attribution 4.0 License. For more information, see https://creativecommons.org/licenses/by/4.0/

This article has been accepted for publication in IEEE Access. This is the author's version which has not been fully edited and content may change prior to final publication. Citation information: DOI 10.1109/ACCESS.2023.3337036

(a)

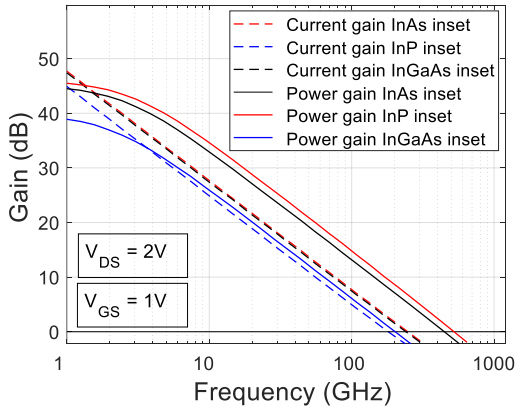

(b)

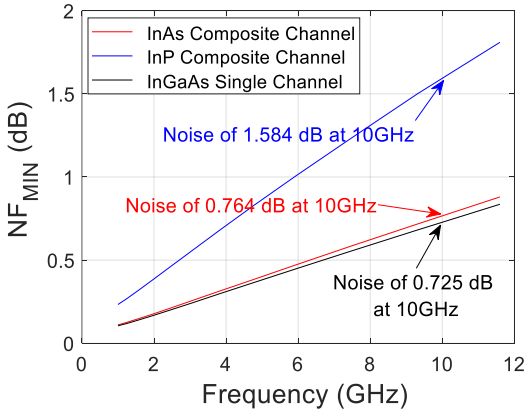

FIGURE 7 (a). Variation of Unilateral Power Gain (dB) and Current Gain (dB) with frequency for different channel inset materials. The dashed curves represent current gain while the solid curves represent power gain. (b). Variation of NF_{MIN} with frequency for different channel inset materials.

Following Fukui's equations (1) and (2), the optimized device structures for AC gain performance and AC noise are expected to be the same. However, due to channel inset effects and impurity scattering, they differ from one another, causing a performance trade-off between gain and noise in the device dimension optimization process.

Pozdnyakov's scattering rate model and polar scattering angle model can be used to determine electron mobility characteristics while accommodating the effects of ionized impurities at various concentrations. Pozdnyakov's scattering rate model models are given in (14) to (17) and Pozdnyakov's angle scattering models are given in (18) and (19) [12].

$$W_j = W_j^{aa} + W_j^{ab} + W_j^{bb} \tag{14}$$

$$W_j^{aa} = 4\pi a^2 n_j I_{aa}\left(\frac{2E(1+\eta E)}{m_d(1+2\eta E)^2}\right)^{\frac{1}{2}} \frac{\Xi^2_{a,j}}{1+f_a} \tag{15}$$

$$W_j^{ab} = 8\pi ab n_j I_{ab}\left(\frac{2E(1+\eta E)}{m_d(1+2\eta E)^2}\right)^{\frac{1}{2}} \times \frac{\Xi_{a,j}\Xi_{b,j}}{f_a - f_b} ln\left(\frac{1+f_a}{1+f_b}\right) \tag{16}$$

$$W_j^{bb} = 4\pi b^2 n_j I_{bb}\left(\frac{2E(1+\eta E)}{m_d(1+2\eta E)^2}\right)^{\frac{1}{2}} \frac{\Xi^2_{b,j}}{1+f_b} \tag{17}$$

where W_j is the scattering rate of electrons by the j-th kind ionized impurities. 'a' and 'b' are the radii of the III-V material's constituent elements. W_j^{aa} denotes scattering between particles of radius 'a', W_j^{ab} denotes scattering between particles of radius 'a' and 'b', and W_j^{bb} denotes scattering between particles of radius 'b'. $\Xi_{a,j}$ and $\Xi_{b,j}$ are two functions such that $\Xi(0) = 1$ and $\Xi(k\to\infty)\to 0$ are true where k is the distance between particles 'a' and 'b.

m_d is the density-of-state electron effective mass and η is the non-parabolicity parameter. 'f_a' and 'f_b' denote the collision frequency of particles 'a' and 'b' respectively.

$$cos(\theta_\rho^{aa}) = 1 - 2\frac{1-\rho}{1+\rho f_a} \tag{18}$$

$$cos(\theta_\rho^{bb}) = 1 - 2\frac{1-\rho}{1+\rho f_b} \tag{19}$$

where θ_ρ^{aa} denotes the scattering angle after collision with a radius 'a' particle and θ_ρ^{bb} denotes the scattering angle after collision with a radius 'b' particle. ρ is the effective charge density while 'f_a' and 'f_b' denote the collision frequency of particles 'a' and 'b' respectively.

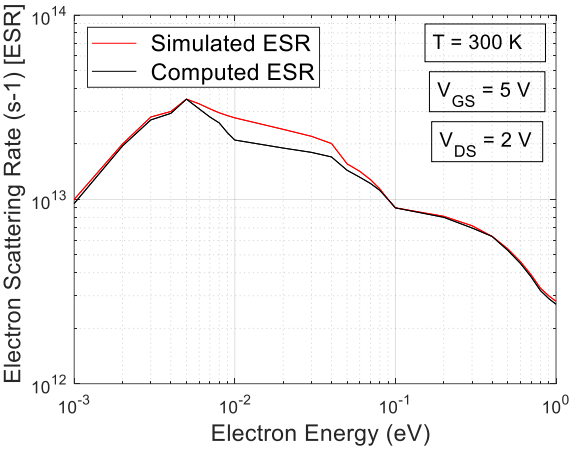

FIGURE 8. Electron Scattering Rate (ESR) variation with Electron Energy. The ESR variation obtained from TCAD simulation was found to match the mathematically computed ESR after accounting for impurity scattering effects within the device.

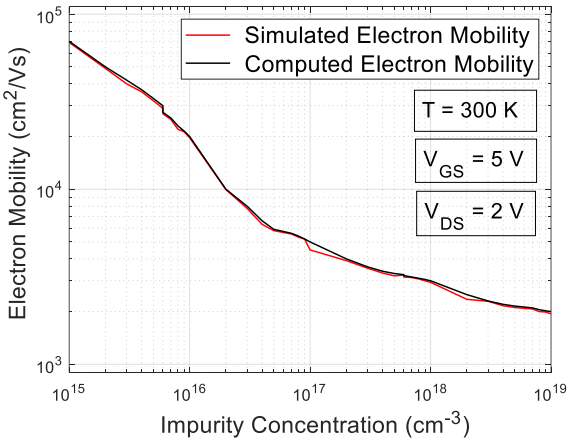

FIGURE 9. Variation of Electron Mobility in the proposed HEMT was found to match the mathematically obtained Electron Mobility only after accounting for impurity scattering effects within the device.

This work is licensed under a Creative Commons Attribution 4.0 License. For more information, see https://creativecommons.org/licenses/by/4.0/

This article has been accepted for publication in IEEE Access. This is the author's version which has not been fully edited and content may change prior to final publication. Citation information: DOI 10.1109/ACCESS.2023.3337036

Applying Pozdnyakov's model to our composite channel HEMT in Fig 8, we observe that the modelled variation of electron scattering rate with impurity concentration matches the simulated electron scattering rate, with low error between the mathematically computed data and the data obtained upon TCAD simulation using ATLAS In Fig 9, we observe the non-linear variation in electron mobility as a consequence of impurity scattering.

IV. SMALL SIGNAL MODELLING AND CIRCUIT INTEGRATION

A. Intrinsic FET model creation using Y parameters

Small signal models help a circuit design engineer easily understand the characteristics and behavior of the device being modelled. Small signal models are used to simplify the analysis of electronic circuits by linearizing nonlinear components. They enable the study of circuit behavior around a bias point, making it easier to analyze and design amplifiers and other signal processing systems.

The S parameter model represents the scattering parameters of a device or circuit. It describes the relationship between incident and reflected waves at the ports, enabling analysis of signal transmission, reflection, and impedance matching in microwave systems. The Y parameter model on the other hand represents the admittance parameters of a two-port network.

The proposed HEMT device can be reduced to an intrinsic FET model using either the S parameter model or using the Y parameter model. The extraction of equivalent circuit parameters using S-parameters, however, is an ill-conditioned problem as there are too many unknowns and not enough equations [34]. Typically, optimization-based techniques are used to solve this problem. However, these procedures may lead to element values with no physical meaning and moreover, the results obtained are deeply influenced by the optimization method chosen. This leads us to use the Y parameter model equations (20)-(23) instead for equivalent circuit parameter extraction [35]-[38].

$$Y_{11} = \frac{j\omega C_{gs}}{1+j\omega C_{gs}R_i} + \frac{j\omega C_{gd}}{1+j\omega C_{gd}R_{gd}} \quad (20)$$

$$Y_{12} = -\frac{j\omega C_{gd}}{1+j\omega C_{gd}R_{gd}} \quad (21)$$

$$Y_{21} = \frac{g_m e^{-j\omega\tau}}{1+j\omega C_{gs}R_i} - \frac{j\omega Cgd}{1+j\omega C_{gd}R_{gd}} \quad (22)$$

$$Y_{22} = \frac{j\omega C_{gd}}{1+j\omega C_{gd}R_{gd}} + j\omega C_{ds} + \frac{1}{R_{ds}} \quad (23)$$

Using (20)-(23), we can solve for each of the equivalent circuit parameters (ECPs) in the equations (24) to (30):

$$R_{gd} = -Re(\frac{1}{Y_{12}}) \quad (24)$$

$$R_i = Re(\frac{1}{Y_{11}+Y_{12}}) \quad (25)$$

$$C_{gd} = \frac{1}{\omega\, Im(\frac{1}{Y_{12}})} \quad (26)$$

$$C_{gs} = -\frac{1}{\omega\, Im(\frac{1}{Y_{11}+Y_{12}})} \quad (27)$$

$$C_{SD} = \frac{Im(Y_{12}+Y_{22})}{\omega} \quad (28)$$

$$g_m = \left|\frac{(Y_{21}-Y_{12})(Y_{11}+Y_{12})}{Im(Y_{11}+Y_{12})}\right| \quad (29)$$

$$\tau = -\frac{Phase\{(Y_{21}-Y_{12})[1+j\frac{Re(Y_{11}+Y_{12})}{Im(Y_{11}+Y_{12})}]\}}{\omega} \quad (30)$$

B. Proposed Temperature and Frequency dependent Intrinsic FET model

Notice that the Y parameters used in this model are not temperature dependent. A critical problem with existing small signal models is that they are not suitable for deep-space or cryogenic applications as these parameters vary with temperature and do not show consistent trends. Using the anomalous electron mobility modelling procedure that was introduced in the device performance section, the effect of ionized impurities creating inconsistent trends at cryogenic temperatures can be modelled accurately. The equivalent circuit parameters obtained can be used to design the intrinsic FET model represented in Fig. 10.

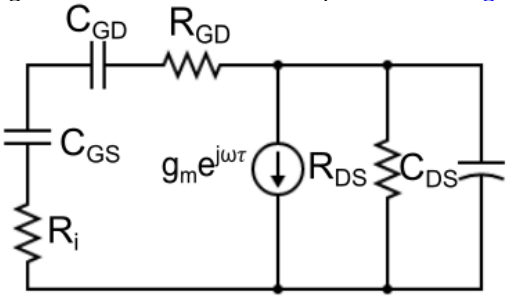

FIGURE 10. Intrinsic FET model using equivalent circuit parameters.

The model being proposed is a temperature dependent Y parameter model and hence, a temperature dependent intrinsic FET model. This proposed model allows one to predict the performance of the device at any intermediate temperature between the simulated data points. Temperature-dependent parameter modeling is vital in designing deep space devices due to the extreme temperature variations encountered. It allows accurate prediction of device performance by accounting for thermal effects on parameters such as resistances, capacitances, and transconductances. The proposed model facilitates proper characterization of the device's behavior over a useful temperature range. The proposed model uses high degree polynomial regression to fit any inconsistent or cyclical trends that are observed in the Y parameter model. The model was fitted to the data using 4th order polynomial regression.

The temperature-dependent equivalent circuit parameter model $Y_{ij}(\theta)$ represents Y_{ij} as a function of temperature. The proposed models, along with corresponding regression characteristics: sum of squares of errors (SSE), R-square, adjusted R-square and Root Mean Squared Error (RMSE) are shown in Figs. 11(a) to (h). The sum of squares error (SSE) is the difference between the observed and predicted values. Lower values of SSE indicate a more accurate

This work is licensed under a Creative Commons Attribution 4.0 License. For more information, see https://creativecommons.org/licenses/by/4.0/

This article has been accepted for publication in IEEE Access. This is the author's version which has not been fully edited and content may change prior to final publication. Citation information: DOI 10.1109/ACCESS.2023.3337036

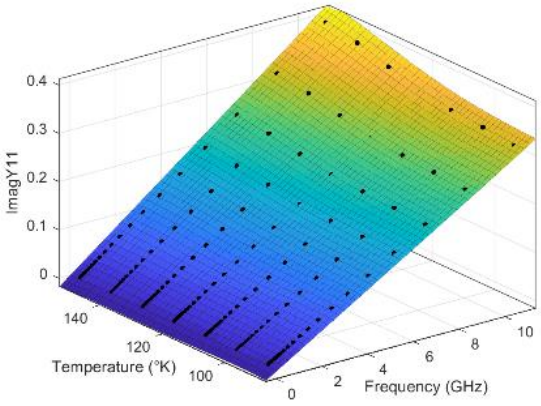

(a) SSE: 8.741e-05 R-square: 0.9999 Adjusted R-square: 0.9999 RMSE: 0.00079

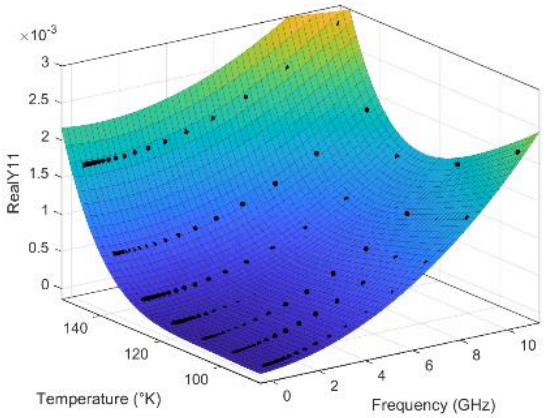

(b) SSE: 4.844e-08 R-square: 0.9993 Adjusted R-square: 0.9992 RMSE: 1.867e-05.

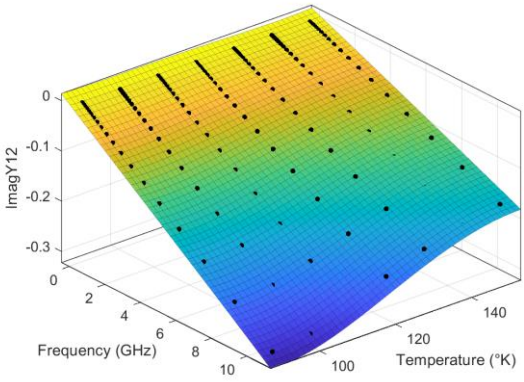

(c) SSE: 2.332e-06 R-square: 0.9897 Adjusted R-square: 0.9886 RMSE: 0.0001295

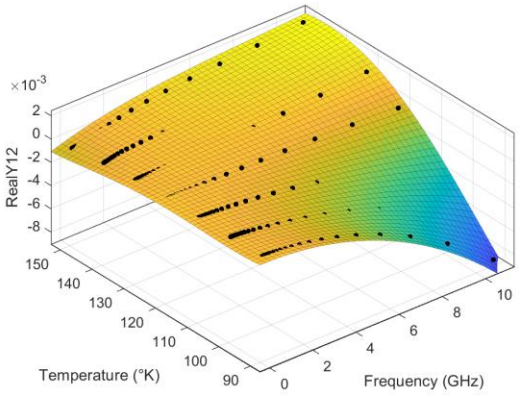

(d) SSE: 5.905e-05 R-square: 0.9999 Adjusted R-square: 0.9999 RMSE: 0.0006518.

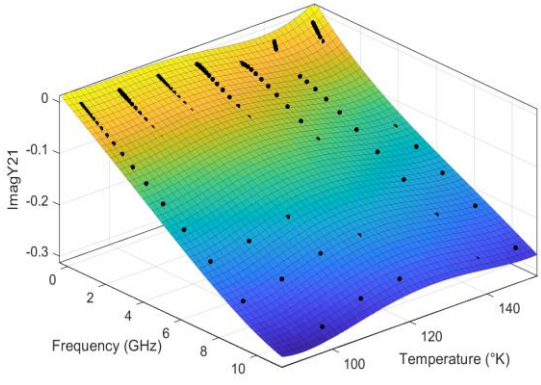

(e) SSE: 0.004584 R-square: 0.9939 Adjusted R-square: 0.9933 RMSE: 0.005743.

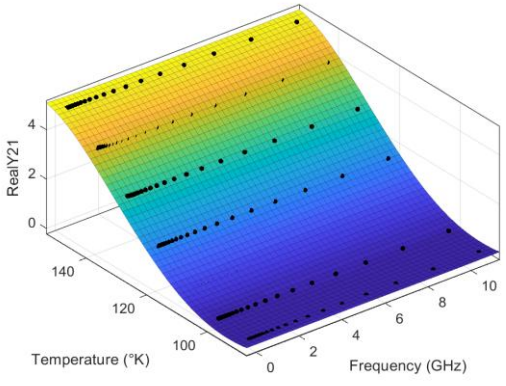

(f) SSE: 0.09077 R-square: 0.9998 Adjusted R-square: 0.9998 RMSE: 0.02555.

This work is licensed under a Creative Commons Attribution 4.0 License. For more information, see https://creativecommons.org/licenses/by/4.0/

This article has been accepted for publication in IEEE Access. This is the author's version which has not been fully edited and content may change prior to final publication. Citation information: DOI 10.1109/ACCESS.2023.3337036

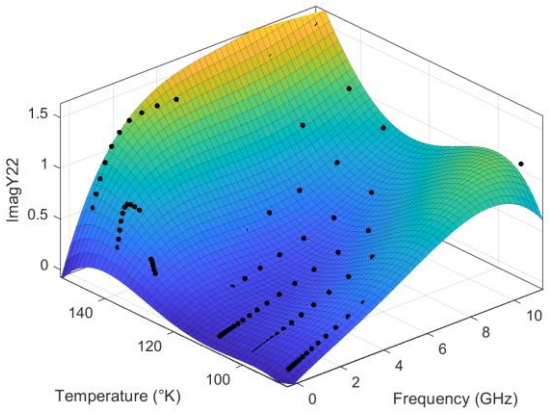

(g) SSE: 2.308 R-square: 0.9997 Adjusted R-square: 0.9997 RMSE: 0.1289.

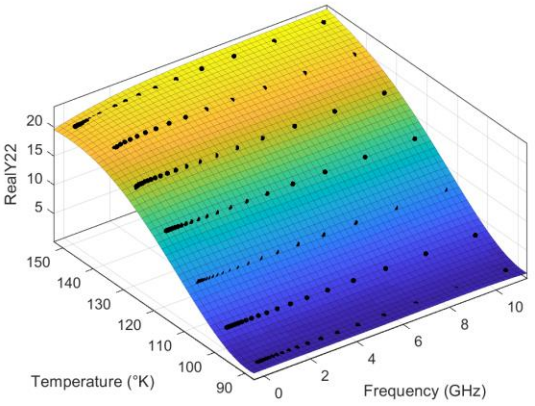

(h) SSE: 1.808 R-square: 0.9153 Adjusted R-square: 0.9068 RMSE: 0.1141

FIGURE 11. Proposed Y-parameter models as a function of Temperature and Frequency obtained using 4th order polynomial regression (a). Im(Y_{11}(f, θ)) (b). Re(Y_{11}(f, θ)) (c). Im(Y_{12}(f, θ)) (d). Re(Y_{12}(f, θ (e). Im(Y_{21}(f, θ)) (f). Re(Y_{21}(f, θ)) (g). Im(Y_{22}(f, θ)) (h). Re (Y_{22}(f, θ)).

regression fit. R-square and adjusted R-square are measures that provide information about the goodness of fit of a model. RMSE is another performance indicator of a regression model. It measures the average difference between values predicted by a model and the actual values. The ECP values obtained using the proposed temperature-and-frequency dependent Y-parameter model are obtained in (31) to (38) as follows:

$$R_{gd} = -Re\left(\frac{1}{Y_{12}(\theta)}\right) \quad (31)$$

$$R_i = Re\left(\frac{1}{Y_{11}(\theta)+Y_{12}(\theta)}\right) \quad (32)$$

$$R_{ds} = \frac{1}{Re(Y_{12}(\theta)+Y_{22}(\theta))} \quad (33)$$

$$C_{gd} = \frac{1}{\omega\, Im\left(\frac{1}{Y_{12}(\theta)}\right)} \quad (34)$$

$$C_{gs} = -\frac{1}{\omega\, Im\left(\frac{1}{Y_{11}(\theta)+Y_{12}(\theta)}\right)} \quad (35)$$

$$C_{SD} = \frac{Im(Y_{12}(\theta)+Y_{22}(\theta))}{\omega} \quad (36)$$

$$g_m = \left|\frac{(Y_{21}(\theta)-Y_{12}(\theta))(Y_{11}(\theta)+Y_{12}(\theta))}{Im(Y_{11}(\theta)+Y_{12}(\theta))}\right| \quad (37)$$

$$\tau = -\frac{Phase\{(Y_{21}(\theta)-Y_{12}(\theta))[1+j\frac{Re(Y_{11}(\theta)+Y_{12}(\theta))}{Im(Y_{11}(\theta)+Y_{12}(\theta))}]\}}{\omega} \quad (38)$$

The equation for parameter variation for the specific HEMT designed is as follows,

$$Yij = p_{00} + p_{10}f + p_{01}\theta + p_{20}f^2 + p_{11}f\theta + p_{02}\theta^2 + p_{30}f^3 + p_{21}f^2\theta + p_{12}f\theta^2 + p_{03}\theta^3 + p_{40}f^4 + p_{31}f^3\theta + p_{22}f^2\theta^2 + p_{13}f\theta^3 + p_{04}\theta^4 \quad (39)$$

where f is the frequency in Hertz, θ is the temperature in degrees kelvin and the coefficients p_{xy} are given in Table 4, Table 5 and Table 6. The coefficients p_{xy} are used to determine the Y parameter equations Real(Y11), Imag(Y11) Real(Y12), Imag(Y12), Real(Y21), Imag(Y21), Real(Y22) and Imag(Y22) as functions of temperature and frequency.

Table 7 demonstrates the variance of ECP values with temperature as determined by the proposed model. The observed trends in R_{GD}, R_i, R_{DS}, C_{GD}, C_{GS} and C_{DS} display a close correspondence to the expected trends, with resistive parameters dropping steadily with a reduction in temperature and capacitive trends displaying varying behavior.

TABLE 4. Coefficient values of p_{00}, p_{10}, p_{01}, p_{20}, p_{11} with 95% confidence bounds.

Parameter/ Coefficient	p_{00}	p_{10}	p_{01}	p_{20}	p_{11}
Real(Y11)	1.40E-04	1.92E-04	7.84E-05	9.30E-05	-8.04E-05
Imag(Y11)	7.72E-02	9.49E-02	6.61E-03	-1.58E-04	8.09E-03
Real(Y12)	-6.26E-05	-2.36E-04	5.07E-04	-7.33E-05	8.10E-04
Imag(Y12)	-5.37E-02	-6.63E-02	1.48E-02	3.42E-05	1.78E-02
Real(Y21)	1.56E+00	1.42E-03	2.24E+00	1.08E-02	-1.52E-02
Imag(Y21)	-5.32E-02	-5.73E-02	-1.60E-02	-1.25E-03	8.71E-03
Real(Y22)	1.33E+01	-3.42E-02	9.67E+00	-1.86E-01	2.47E-01
Imag(Y22)	1.56E-01	1.68E-02	2.84E-01	-4.16E-02	-8.13E-02

TABLE 5. Coefficient values of p_{02}, p_{30}, p_{21}, p_{12}, p_{03} with 95% confidence bounds.

Parameter/ Coefficient	p_{02}	p_{30}	p_{21}	p_{12}	p_{03}
Real(Y11)	2.36E-04	-3.32E-06	-3.93E-06	1.08E-05	1.95E-04
Imag(Y11)	3.94E-03	-8.43E-05	-3.89E-05	1.58E-03	-3.96E-04
Real(Y12)	-2.35E-04	2.91E-05	8.94E-05	5.50E-05	-1.09E-04
Imag(Y12)	-2.12E-03	7.98E-05	-2.02E-04	2.07E-05	-1.95E-03
Real(Y21)	5.81E-01	-7.97E-03	1.12E-02	-9.59E-03	-2.76E-01
Imag(Y21)	-2.42E-02	-2.20E-03	5.56E-03	-1.03E-02	4.32E-03
Real(Y22)	-1.69E+00	1.31E-01	-2.29E-01	2.56E-01	-1.27E+00
Imag(Y22)	3.94E-01	9.38E-02	-1.56E-01	1.87E-01	1.04E-04

TABLE 6. Coefficient values of p_{40}, p_{13}, p_{22}, p_{13}, p_{04} with 95% confidence bounds.

Parameter/ Coefficient	p_{40}	p_{31}	p_{22}	p_{13}	p_{04}
Real(Y11)	8.23E-07	-2.09E-06	1.48E-05	6.77E-06	5.26E-05
Imag(Y11)	7.03E-05	2.48E-05	-5.46E-06	-5.07E-04	-1.12E-03
Real(Y12)	-4.53E-06	2.75E-05	-1.59E-04	-5.17E-05	8.84E-05
Imag(Y12)	-3.57E-05	5.74E-05	-6.59E-05	-2.42E-03	9.36E-04
Real(Y21)	1.51E-03	-2.29E-03	2.16E-03	-7.64E-06	-8.23E-02
Imag(Y21)	4.38E-04	-1.60E-03	3.34E-03	-2.75E-03	6.09E-03
Real(Y22)	-2.32E-02	4.60E-02	-6.08E-02	6.16E-02	3.83E-01
Imag(Y22)	-1.91E-02	4.36E-02	-6.93E-02	6.85E-02	-7.01E-02

This work is licensed under a Creative Commons Attribution 4.0 License. For more information, see https://creativecommons.org/licenses/by/4.0/

This article has been accepted for publication in IEEE Access. This is the author's version which has not been fully edited and content may change prior to final publication. Citation information: DOI 10.1109/ACCESS.2023.3337036

TABLE 7. The obtained ECP values using our proposed intrinsic FET model at 350K, 300K, 250K, 200K, 150K and 100K at 1 GHz.

ECP/ Temperature	350K	300K	250K	200K	150K	100K
R_{GD} (Ω.mm)	7.48	5.59	4.15	1.14	0.78	0.57
R_i (Ω.mm)	5.89	4.22	3.76	2.63	1.95	1.11
R_{DS} (Ω.mm)	12.0	10.1	8.72	4.82	2.55	1.26
C_{GD} (fF/mm)	10.08	11.09	13.14	23.71	46.93	90.71
C_{GS} (fF/mm)	126.6	121.3	113.4	102.9	61.2	2.06
C_{DS} (fF/mm)	304.5	299.3	286.6	273.9	201.1	130.5

C. Comparison of estimated ECP values with extracted ECP values

To test the accuracy of the ECP values obtained using the Y parameter model, the ECP values estimated using the Y parameter model at different temperatures have been compared with the actual ECP values extracted using TCAD simulation.

The estimated capacitance ECPs are obtained between 1 GHz and 10 GHz using (24) – (26) for 19 different frequencies. The simulated capacitance ECPs are obtained by solving drift-diffusion equations and obtaining the corresponding charge and potential profiles to estimate capacitance between the electrodes.

A comparative analysis of the estimated ECP capacitance values with extracted ECP capacitance values at 300 K, 200 K and 100 K are presented in Figs.12(a) to (i). The gate-source capacitance (C_{GS}) and source-drain capacitance (C_{SD}) were observed to drop off at cryogenic temperatures due to the shrinking of the depletion region at the source and drain terminals. The gate-drain capacitance (C_{GD}) on the other hand was found to increase with a decrease in temperature owing to reduced carrier concentration at the gate Schottky contact. With fewer carriers in the channel region, the electrostatic influence of the gate electrode on the carriers becomes more pronounced, leading to an increase in gate-drain capacitance.

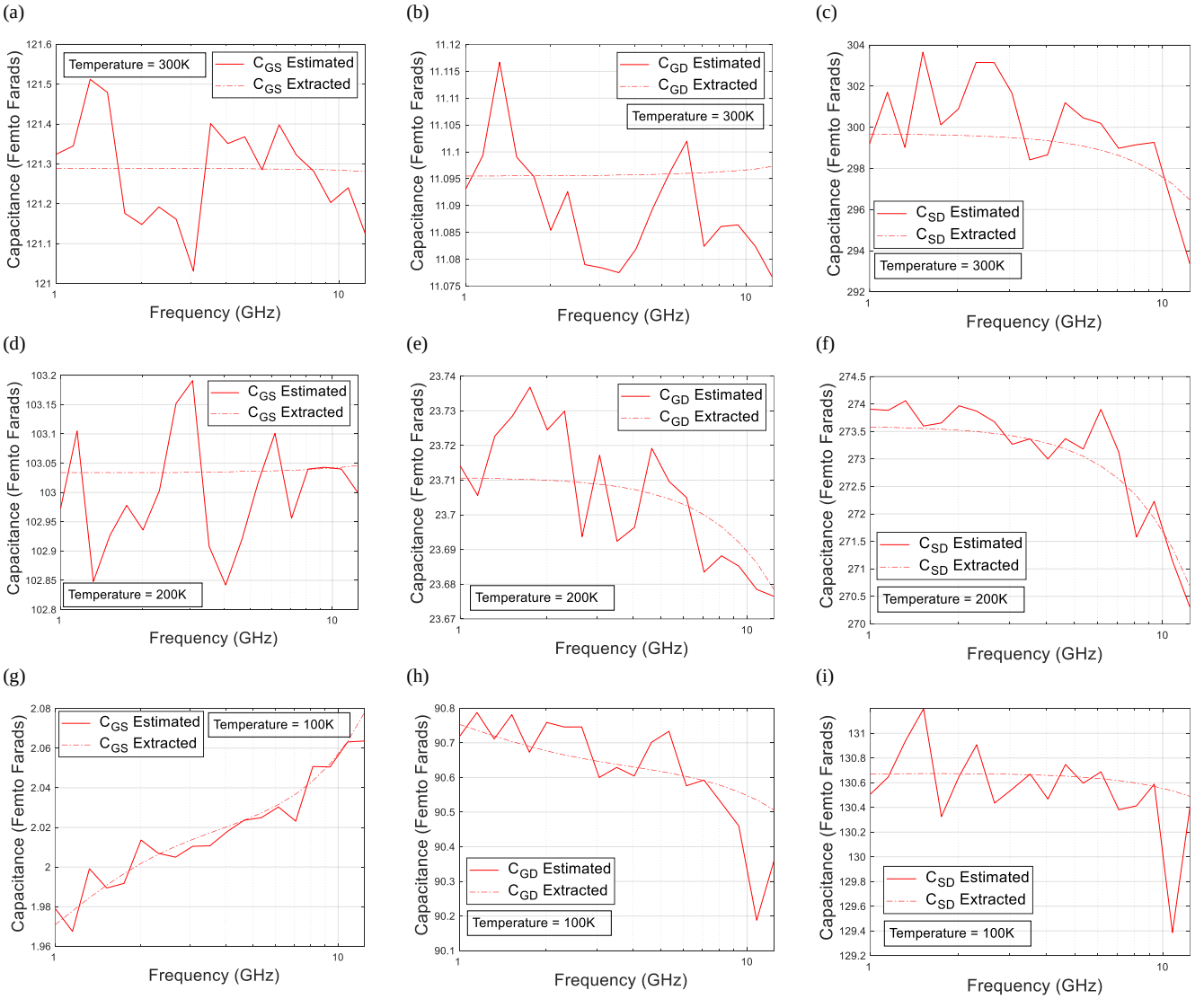

FIGURE 12 (a).Comparison of estimated and extracted C_{GS} at 300 K. (b) Comparison of estimated and extracted C_{GD} at 300 K. (c) Comparison of estimated and extracted C_{SD} at 300 K. (d) Comparison of estimated and extracted C_{GS} at 200 K. (e) Comparison of estimated and extracted C_{GD} at 200 K. (f) Comparison of estimated and extracted C_{SD} at 100 K. (g) Comparison of estimated and extracted C_{GS} at 200 K. (h) Comparison of estimated and extracted C_{GD} at 100 K. (i) Comparison of estimated and extracted C_{SD} at 100 K.

This work is licensed under a Creative Commons Attribution 4.0 License. For more information, see https://creativecommons.org/licenses/by/4.0/

This article has been accepted for publication in IEEE Access. This is the author's version which has not been fully edited and
content may change prior to final publication. Citation information: DOI 10.1109/ACCESS.2023.3337036

D. Device Interfacing and Circuit Integration

The proposed InP HEMT device and the associated model can be made to interact with other electronic components in an integrated circuit to achieve multiple functions.

The proposed device's fast switching speed and high amplification can be used to realize the switching components S_i and operational amplifiers OP_i. The performance of multimodal generalization and differentiation associative memory circuits proposed in [39] and bionic emotion modules proposed in [40] can be enhanced using the proposed HEMT device. The circuit can be realized using HEMT, which has been shown using a simplified HEMT structure in Fig. 13.

Further, due to the good cryogenic performance of the device, these circuits can be used to realize associative memory and bionic emotion modules in deep-space environments. The proposed InP HEMT can also be integrated into monolithic integrated circuits to realize amplifiers, mixers and multipliers [41] operating in the millimetre wave and early terahertz band range for deep-space applications.

V. FABRICATION PROCESS

InP HEMT devices are commonly fabricated using 3-inch InP wafers. The main processing steps in InP HEMT fabrication are mesa etching, metal contact establishment, passivation and pad metallization. The step-by-step fabrication procedure is explained and shown in Fig. 14.

A. Mesa Etching: Electrical isolation of the HEMT from other devices on the InP wafer is done by wet etching of the InGaAs, InAs and InAlAs layers using a H_2O_2:H_3PO_4:H_2O (1:1:25) solution. The InP etch stop layer is etched separately using a HCl:H_2O (3:2) solution. For forming gate recess structures using wet etching, citric acid/H_2O_2 [42] or phosphoric acid/H_2O_2 [43] is used. A substrate temperature of 200 C – 600 C is used in the InP HEMT fabrication process, although lower temperatures within this band are preferred to reduce the possibility of fluorine contamination [42]. Limiting substrate temperature within 250 C and 300 C allows for desirable wet etching of the InP HEMT but also considerably reduces fluorine contamination effects.

B. Source and Drain contact formation: Source and drain contacts of InP HEMTs are typically formed using metal amalgams such as AuGeNi [44], TiMoTiPtAu [45], NiGeAuGeNi [46], TiPtAu [47], NiGeAu/Ge/NiAu [48], NiGeAu [49] and AuGeNiAu [50]. The DC and RF performance of InP HEMTs can be considerably improved upon annealing treatments during contact formatin. For InP devices, buried platinum annealing treatment is done in nitrogen-rich environments at a temperature of 250 C – 600 C. The required process time varies between 30 s and 15 mins depending on the dimensions of the device involved [51].

C. Gate contact establishment: Gate electrodes are typically formed using metal amalgamations of Ti, Pt, Au, Ge, Ni and Mo [52]-[53]. The parasitics associated with the gate stem of an InP HEMT are considerably lowered with a gate stem height of over 0.25µm. Two step or three step gate recess processes are employed to fabricate InP FETs with gate lengths less than 50 nm. The usage of multiple gate recess steps allows the fabrication of InP HEMTs with gate-channel distances up to 4 nm when compared to conventional gate recess processes. Due to thermal reactions between the gate metal and the semiconductor surface, 'gate sinking' takes place which is a major gate fabrication challenge. An electron beam lithographic process is generally used to recess the gate to a depth beneath the surface of the device. For gate lengths of 30 nm and below, fullerene introduced nano-composite beam fabrication techniques are employed [54].

D. Passivation and Doping: Passivation of InP HEMTs is performed using the plasma enhanced chemical vapor deposition process. Si_3N_4 is mainly used for surface passivation because of its low permittivity. A temperature of less than 300 C is generally used to passivate Si_3N_4. Passivation using low permittivity materials can be used to reduce parasitic capacitance but also worsens the cut-off frequency of the device. Doping within an InP device can be performed using four different doping procedures. Single side Si-planar doping [55] and single side Si-δ-doping [56] is typically used above the channel region, double side Si-planar-doping [57] is used below the channel region and double-sided Si-δ-doping [45] can be used both above and below the channel region.

Double sided doping techniques can minimize the effects of impact ionization within the channel and consequently minimize kink effects observed in the output characteristics. The epitaxial growth process of a δ-doped structure such as that in the proposed HEMT devices differs from standard growth procedures. The creation of a δ-doped layer requires a lower substrate temperature in order to reduce surface segregation reactions of silicon atoms in the InAlAs layer.

E. Pad metallization: The passivation layer is first removed in the pad metallization regions using Si_3N_4 by reactive ion etching or using aluminium oxide. The pad metal stack is subsequently deposited by electron beam evaporation.

This work is licensed under a Creative Commons Attribution 4.0 License. For more information, see https://creativecommons.org/licenses/by/4.0/

This article has been accepted for publication in IEEE Access. This is the author's version which has not been fully edited and
content may change prior to final publication. Citation information: DOI 10.1109/ACCESS.2023.3337036

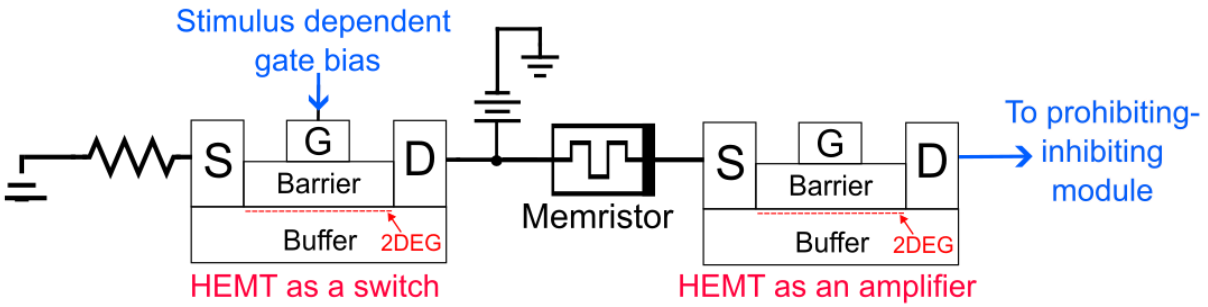

FIGURE 13. Integration of the proposed HEMT device in the logical judgement module of a bionic emotion module.

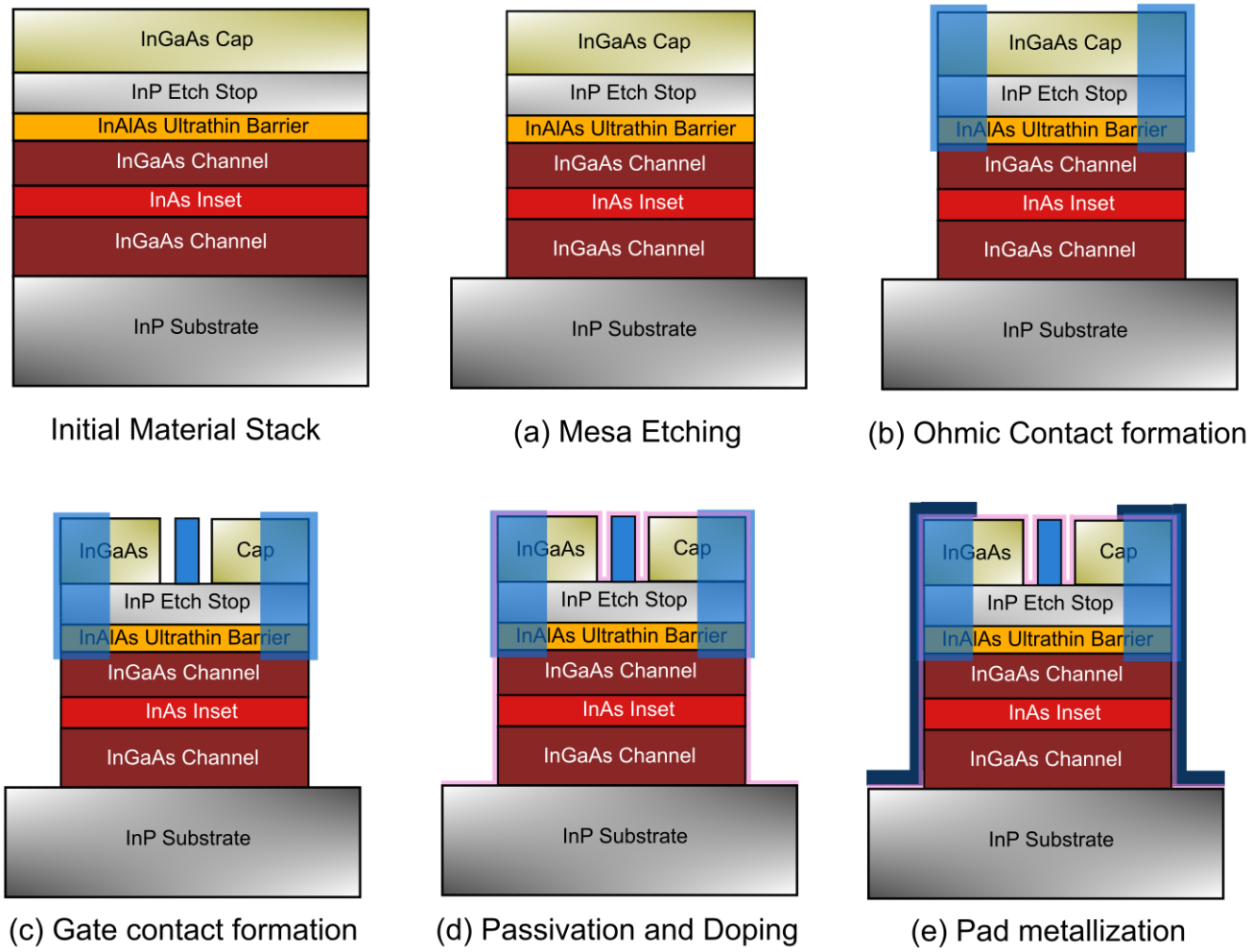

FIGURE 14. Step-by-step fabrication procedure of the proposed InP HEMT (a) Mesa Etching (b) Ohmic contact formation (c) Gate contact formation (d) Passivation and doping, and (e) Pad metallization.

VI. CONCLUSION

In our work, we have designed a novel metamorphic InP HEMT for cryogenic applications which exhibits f_T/f_{MAX} figures of 247.2 GHz/ 526.0 GHz at 298 K, 168 GHz/ 152 GHz at 150 K and 5.02 GHz/ 10.01 GHz at 90 K. We subsequently proposed a small signal model which accurately predicts ECPs within 0.1% of the empirically extracted ECPs. The unique structural topology and material selection in our work was presented and justified with the performance incentives of each design decision such as the ultrathin barrier layer and composite channel explicitly explained. This device was designed in response to address the acute demand for devices with high f_T/f_{MAX}, and favorable noise characteristics across a wide temperature range in the context of deep-space and cryogenic applications. The performance characteristics of the proposed device indicate that is well suited for LNA, sensors and detectors, radio astronomy, quantum computers and other cryogenic RF applications.

This work is licensed under a Creative Commons Attribution 4.0 License. For more information, see https://creativecommons.org/licenses/by/4.0/

This article has been accepted for publication in IEEE Access. This is the author's version which has not been fully edited and
content may change prior to final publication. Citation information: DOI 10.1109/ACCESS.2023.3337036

REFERENCES

[1] Y. Wei, M. M. Hossain and H. A. Mantooth, "Comparisons and Evaluations of Silicon and Wide Band Gap Devices at Cryogenic Temperature," in *IEEE Transactions on Industry Applications*, vol. 59, no. 2, pp. 1982-1994, March-April 2023, doi: 10.1109/TIA.2022.3225370.

[2] Kim, Wonjong, et al., "Doping challenges and pathways to industrial scalability of III–V nanowire arrays", *Applied Physics Reviews* 8.1 (2021).

[3] L. Nela, N. Perera, C. Erine and E. Matioli, "Performance of GaN Power Devices for Cryogenic Applications Down to 4.2 K," in *IEEE Transactions on Power Electronics*, vol. 36, no. 7, pp. 7412-7416, July 2021, doi: 10.1109/TPEL.2020.3047466.

[4] E. Cha, N. Wadefalk, G. Moschetti, A. Pourkabirian, J. Stenarson and J. Grahn, "InP HEMTs for Sub-mW Cryogenic Low-Noise Amplifiers," in *IEEE Electron Device Letters*, vol. 41, no. 7, pp. 1005-1008, July 2020, doi: 10.1109/LED.2020.3000071.

[5] I. Harrysson Rodrigues and A. Vorobiev, "Low-Field Mobility and High-Field Velocity of Charge Carriers in InGaAs/InP High-Electron-Mobility Transistors," in *IEEE Transactions on Electron Devices*, vol. 69, no. 4, pp. 1786-1791, April 2022, doi: 10.1109/TED.2022.3147733.

[6] F. Thome, F. Schäfer, S. Türk, P. Yagoubov and A. Leuther, "A 67–116-GHz Cryogenic Low-Noise Amplifier in a 50-nm InGaAs Metamorphic HEMT Technology," in *IEEE Microwave and Wireless Components Letters*, vol. 32, no. 5, pp. 430-433, May 2022, doi: 10.1109/LMWC.2021.3134462.

[7] Domange, J., et al. "Quantum efficiency for electron-hole pair generation by infrared irradiation in germanium cryogenic detectors." *AIP Conference Proceedings*, vol. 1185, no. 1. American Institute of Physics, 2009.

[8] Bardin, Joseph C., "Cryogenic low-noise amplifiers: Noise performance and power dissipation", *IEEE Solid-State Circuits Magazine*, 13.2 (2021): 22-35.

[9] J. Millán, P. Godignon, X. Perpiñà, A. Pérez-Tomás and J. Rebollo, "A Survey of Wide Bandgap Power Semiconductor Devices," in *IEEE Transactions on Power Electronics*, vol. 29, no. 5, pp. 2155-2163, May 2014, doi: 10.1109/TPEL.2013.2268900.

[10] S. K. Mazumder et al., "Overview of Wide/Ultra-Wide Bandgap Power Semiconductor Devices for Distributed Energy Resources," in *IEEE Journal of Emerging and Selected Topics in Power Electronics*, doi: 10.1109/JESTPE.2023.3277828.

[11] Oxley, C. H. "Calculation of minimum noise figure using the simple Fukui equation for gallium nitride (GaN) HEMTs." *Solid-State Electronics*, 45.5 (2001): 677-682.

[12] Pozdnyakov, D., "Scattering of electrons by ionized impurities in semiconductors: quantum-mechanical approach to third body exclusion", *Journal of Computational Electronics*, 13, 338–351 (2014). https://doi.org/10.1007/s10825-013-0538-8

[13] S. Huang et al., "High Uniformity Normally-OFF GaN MIS-HEMTs Fabricated on Ultra-Thin-Barrier AlGaN/GaN Heterostructure," in *IEEE Electron Device Letters*, vol. 37, no. 12, pp. 1617-1620, Dec. 2016, doi: 10.1109/LED.2016.2617381.

[14] Y. Kim, H. Park and S. Yoo, "High-Efficiency 28-/39-GHz Hybrid Transceiver Utilizing Si CMOS and GaAs HEMT for 5G NR Millimeter-Wave Mobile Applications," in *IEEE Solid-State Circuits Letters*, vol. 6, pp. 1-4, 2023, doi: 10.1109/LSSC.2022.3233907.

[15] Y. Wei, M. M. Hossain and H. A. Mantooth, "Comparisons and Evaluations of Silicon and Wide Band Gap Devices at Cryogenic Temperature," in *IEEE Transactions on Industry Applications*, vol. 59, no. 2, pp. 1982-1994, March-April 2023, doi: 10.1109/TIA.2022.3225370.

[16] E. Cha, N. Wadefalk, G. Moschetti, A. Pourkabirian, J. Stenarson and J. Grahn, "InP HEMTs for Sub-mW Cryogenic Low-Noise Amplifiers," in *IEEE Electron Device Letters*, vol. 41, no. 7, pp. 1005-1008, July 2020, doi: 10.1109/LED.2020.3000071.

[17] J. Gong, X. Chen, W. He, A. Altaf, A. Hu and J. Miao, "A V-Band Integrated Receiver Front-End Based on 0.15 μm GaAs pHEMT Process for Passive Millimeter-Wave Imaging," in *IEEE Access*, vol. 10, pp. 59933-59941, 2022, doi: 10.1109/ACCESS.2022.3175367.

[18] E. Cha et al., "Optimization of Channel Structures in InP HEMT Technology for Cryogenic Low-Noise and Low-Power Operation," in *IEEE Transactions on Electron Devices*, vol. 70, no. 5, pp. 2431-2436, May 2023, doi: 10.1109/TED.2023.3255160.

[19] J. Li, A. Pourkabirian, J. Bergsten, N. Wadefalk and J. Grahn, "Influence of Spacer Thickness on the Noise Performance in InP HEMTs for Cryogenic LNAs," in *IEEE Electron Device Letters*, vol. 43, no. 7, pp. 1029-1032, July 2022, doi: 10.1109/LED.2022.3178613.

[20] F. Thome, F. Schäfer, S. Türk, P. Yagoubov and A. Leuther, "A 67–116-GHz Cryogenic Low-Noise Amplifier in a 50-nm InGaAs Metamorphic HEMT Technology," in *IEEE Microwave and Wireless Components Letters*, vol. 32, no. 5, pp. 430-433, May 2022, doi: 10.1109/LMWC.2021.3134462.

[21] ATessmann et al., "20-nm In0.8Ga0.2As MOSHEMT MMIC Technology on Silicon," in *IEEE Journal of Solid-State Circuits*, vol. 54, no. 9, pp. 2411-2418, Sept. 2019, doi: 10.1109/JSSC.2019.2915161

[22] Raghuveera, E., G. Purnachandra Rao, and Trupti Ranjan Lenka. "Prospects of III–V Semiconductor-Based High Electron Mobility Transistors (HEMTs) Towards Emerging Applications." *International Conference on Micro/Nanoelectronics Devices, Circuits and Systems*. Singapore: Springer Nature Singapore, 2023.

[23] AZamora et al., "A Submillimeter Wave InP HEMT Multiplier Chain," in *IEEE Microwave and Wireless Components Letters*, vol. 25, no. 9, pp. 591-593, Sept. 2015, doi: 10.1109/LMWC.2015.2451364.

[24] W. R. Deal et al., "Low Noise Amplification at 0.67 THz Using 30 nm InP HEMTs," in *IEEE Microwave and Wireless Components Letters*, vol. 21, no. 7, pp. 368-370, July 2011, doi: 10.1109/LMWC.2011.2143701.

[25] D. C. Ruiz, T. Saranovac, D. Han, O. Ostinelli and C. R. Bolognesi, "New GaInAs/InAs/InP Composite Channels for mm-Wave Low-Noise InP HEMTs," 2019 *IEEE BiCMOS and Compound semiconductor Integrated Circuits and Technology Symposium* (BCICTS), Nashville, TN, USA, 2019, pp. 1-4, doi: 10.1109/BCICTS45179.2019.8972710.

[26] D. C. Ruiz et al., "InAs Channel Inset Effects on the DC, RF, and Noise Properties of InP pHEMTs," in *IEEE Transactions on Electron Devices*, vol. 66, no. 11, pp. 4685-4691, Nov. 2019, doi: 10.1109/TED.2019.2940638.

[27] L. Liu, A. R. Alt, H. Benedickter and C. R. Bolognesi, "InP-HEMT X-band Low-Noise Amplifier With Ultralow 0.6-mW Power Consumption," in *IEEE Electron Device Letters*, vol. 33, no. 2, pp. 209-211, Feb. 2012, doi: 10.1109/LED.2011.2176713.

[28] Crupi, G.; Schreurs, D.M.M.-P.; Caddemi, A. Effects of Gate-Length Scaling on Microwave MOSFET Performance. *Electronics* 2017, 6, 62. https://doi.org/10.3390/electronics6030062

[29] Pfützenreuter, Daniel, et al. "Confinement of Electrons at the LaInO3/BaSnO3 Heterointerface." *Advanced Materials Interfaces* 9.35 (2022): 2201279.

[30] Aydinoglu, H. S., et al. "Nonlinear optical properties in AlxGa1-xAs/GaAs double-graded quantum wells: The effect of the structure parameter, static electric, and magnetic field." *Solid State Communications* 342 (2022): 114647.

[31] Dresselhaus, Mildred, et al. "Two dimensional electron gas, quantum wells and semiconductor superlattices." *Solid State Properties: From Bulk to Nano* (2018): 247-274.

[32] Cipriano, Luis A., et al. "Quantum confinement in group III–V semiconductor 2D nanostructures." *Nanoscale* 12.33 (2020): 17494-17501.

[33] Li, Kexin, et al. "Compact modeling of gate leakage phenomenon in GaN HEMTs." 2020 *International Conference on Simulation of Semiconductor Processes and Devices* (SISPAD). IEEE, 2020.

[34] Z. Feng et al., "An Accurate Model for InP HEMT Small-Signal Equivalent Circuit Based on EM Simulation," in *IEEE Transactions*

This work is licensed under a Creative Commons Attribution 4.0 License. For more information, see https://creativecommons.org/licenses/by/4.0/

This article has been accepted for publication in IEEE Access. This is the author's version which has not been fully edited and
content may change prior to final publication. Citation information: DOI 10.1109/ACCESS.2023.3337036

on Electron Devices, vol. 70, no. 3, pp. 934-940, March 2023, doi: 10.1109/TED.2023.3235709.

[35] G. Crupi and D. M. M.-P. Schreurs, Microwave De-Embedding: From Theory to Applications, Oxford, U.K.:Academic, 2013.

[36] L. F. Tiemeijer, R. J. Havens, A. B. M. Jansman and Y. Bouttement, "Comparison of the 'pad-open-short' and 'open-short-load' deembedding techniques for accurate on-wafer RF characterization of high-quality passives", *IEEE Trans. Microw. Theory Techn*., vol. 53, no. 2, pp. 723-729, Feb. 2005.

[37] N. Rorsman, M. Garcia, C. Karlsson and H. Zirath, "Accurate small-signal modeling of HFET's for millimeter-wave applications", *IEEE Trans. Microw. Theory Techn.*, vol. 44, no. 3, pp. 432-437, Mar. 1996.

[38] G. Crupi, D. M. M.-P. Schreurs, A. Caddemi, A. Raffo and G. Vannini, "Investigation on the non-quasi-static effect implementation for millimeter-wave FET models", *Int. J. RF Microw. Comput.-Aided Eng.*, vol. 20, no. 1, pp. 87-93, Jan. 2010.

[39] J. Sun, Y. Wang, P. Liu, S. Wen and Y. Wang, "Memristor-Based Neural Network Circuit With Multimode Generalization and Differentiation on Pavlov Associative Memory," in *IEEE Transactions on Cybernetics*, vol. 53, no. 5, pp. 3351-3362, May 2023, doi: 10.1109/TCYB.2022.3200751.

[40] J. Sun, Y. Wang, P. Liu, S. Wen and Y. Wang, "Memristor-Based Circuit Design of PAD Emotional Space and Its Application in Mood Congruity," in *IEEE Internet of Things Journal*, vol. 10, no. 18, pp. 16332-16342, 15 Sept.15, 2023, doi: 10.1109/JIOT.2023.3267778.

[41] W. R. Deal, K. Leong, W. Yoshida, A. Zamora and X. B. Mei, "InP HEMT integrated circuits operating above 1,000 GHz," 2016 *IEEE International Electron Devices Meeting* (IEDM), San Francisco, CA, USA, 2016, pp. 29.1.1-29.1.4, doi: 10.1109/IEDM.2016.7838502.

[42] Endoh, Akira, et al. "InP-based high electron mobility transistors with a very short gate-channel distance." *Japanese journal of applied physics* 42.4S (2003): 2214.

[43] Wang, Li-Dan, et al. "100-nm T-gate InAlAs/InGaAs InP-based HEMTs with fT= 249 GHz and fmax= 415 GHz." *Chinese Physics B* 23.3 (2014): 038501.

[44] Moran, D. A. J., et al. "Self-aligned T-gate InP HEMT realisation through double delta doping and a non-annealed ohmic process." *Microelectronic engineering* 73 (2004): 814-817.

[45] Yun, Do-Young, et al. "Impact of the source-to-drain spacing on the DC and RF characteristics of InGaAs/InAlAs high-electron mobility transistors." *IEEE Electron Device Letters* 39.12 (2018): 1844-1847.

[46] Li, Qiang, et al. "InP lattice-matched HEMT with regrown Source/Drain by MOCVD." IPRM 2011-23rd *International Conference on Indium Phosphide and Related Materials*. IEEE, 2011.

[47] Mei, Xiaobing, et al. "First demonstration of amplification at 1 THz using 25-nm InP high electron mobility transistor process." *IEEE Electron Device Letters* 36.4 (2015): 327-329.

[48] Zhong, Yinghui, et al. "Impact of the lateral width of the gate recess on the DC and RF characteristics of InAlAs/InGaAs HEMTs." *Journal of Semiconductors* 33.5 (2012): 054007.

[49] Kim, Dae-Hyun, and Jesús A. Del Alamo. "30-nm InAs PHEMTs with f T= 644 GHz and f max= 681 GHz." *Institute of Electrical and Electronics Engineers*, 2010.

[50] Fukuyama, Hiroyuki, et al. "Photoreceiver module using an InP HEMT transimpedance amplifier for over 40 Gb/s." *IEEE journal of solid-state circuits* 39.10 (2004): 1690-1696.

[51] J. Ajayan, D. Nirmal, Ribu Mathew, Dheena Kurian, P. Mohankumar, L. Arivazhagan, D. Ajitha, A critical review of design and fabrication challenges in InP HEMTs for future terahertz frequency applications, *Materials Science in Semiconductor Processing*, Volume 128, 2021, 105753, ISSN 1369-8001, https://doi.org/10.1016/j.mssp.2021.105753.

[52] Kim, Dae-Hyun, and Jesus A. del Alamo. "30 nm E-mode InAs PHEMTs for THz and future logic applications." 2008 *IEEE International Electron Devices Meeting*. IEEE, 2008.

[53] Yao, Jing-Neng, et al. "Communication—Potential of the π-gate InAs HEMTs for high-speed and low-power logic applications." *ECS Journal of Solid State Science and Technology* 8.6 (2019): P319.

[54] Suemitsu, Tetsuya Suemitsu Tetsuya, et al. "30-nm-gate InP-based lattice-matched high electron mobility transistors with 350 GHz cutoff frequency." *Japanese journal of applied physics* 38.2B (1999): L154.

[55] Zhong, Yinghui, et al. "Impact of the lateral width of the gate recess on the DC and RF characteristics of InAlAs/InGaAs HEMTs." *Journal of Semiconductors* 33.5 (2012): 054007.

[56] Kim, Dae-Hyun, et al. "Logic Suitability of 50-nm In0.7Ga0.3As HEMTs for Beyond-CMOS Applications." *IEEE transactions on electron devices* 54.10 (2007): 2606-2613.

[57] Takahashi, Tsuyoshi, et al. "Enhancement of fMAX to 910 GHz by Adopting Asymmetric Gate Recess and Double-Side-Doped Structure in 75-nm-Gate InAlAs/InGaAs HEMTs." *IEEE Transactions on Electron Devices* 64.1 (2016): 89-95.

Soumak Nandi is currently pursuing his B.Tech degree in Electronics and Communication Engineering from Birla Institute of Technology, Mesra, Ranchi, India. His research interests include high-speed devices, high-electron-mobility-transistors, III-V semiconductor devices, low-power VLSI design and integration of emerging semiconductor devices in RF & high-power applications.

Shashank Kumar Dubey received the B.Tech degree in electronics and communications engineering from APJ Abdul Kalam Technical University (APJAKTU), Lucknow, Uttar Pradesh, India, in 2014. He received ME degree in electronics and communication engineering (wireless communication) from Birla Institute of Technology Mesra, Ranchi, India, in 2018. He received his PhD degree from Birla Institute of Technology Mesra, Ranchi, India in 2023. He is currently working as an assistant professor at G. Pullaiah College of Engineering and Technology, Kurnool, Andhra Pradesh, India.

His broad research area encompasses VLSI, microelectronics, and nanoelectronics. His specific research interests include VLSI design/CAD for nanoscale silicon and III-V technologies which center around the emerging nanoelectronics and high speed devices and circuits like, HEMT, SRAM, RRAM etc. He has authored/ coauthored more than 32 research articles in reputed journals, book chapter and international conferences. He has published one patent in IPR and filed one patent in IPR.

Mukesh Kumar completed his B.Tech. in Electronics and Communication Engineering at the National Institute of Technology, Patna, India, in 2013. Subsequently, he obtained his M. Tech. in Digital Communication Engineering from Swami Vivekanand University, Sagar, India, in 2015. Currently, he is pursuing his Ph.D. at Birla Institute of Technology, Mesra, Ranchi, Jharkhand, India. His research interests are diverse and encompass III-V semiconductor devices, low-power VLSI design, Microelectronics, and nanoelectronics. He has authored/ coauthored 4 research articles in book chapter and international conferences.

Amit Krishna Dwivedi (GS'14-M'21) is currently working as an Assistant Professor in Electrical and Electronic Engineering at the School of Engineering, University of Warwick, UK. Dr. Dwivedi received both the B.Tech. and the M.E. degrees in Electronics Engineering from India, in 2012 and 2015, respectively, and the Ph.D. degree in Electrical and Electronic Engineering from Imperial College London, UK.

Before joining the University of Warwick, Dr.

This work is licensed under a Creative Commons Attribution 4.0 License. For more information, see https://creativecommons.org/licenses/by/4.0/

This article has been accepted for publication in IEEE Access. This is the author's version which has not been fully edited and
content may change prior to final publication. Citation information: DOI 10.1109/ACCESS.2023.3337036

Dwivedi was with the Department of Engineering as a Lecturer/Assistant Professor in Electronic and Electrical Engineering at Manchester Metropolitan University, Manchester, UK, and as a researcher with the Diagnostic Imaging Center, Kuopio University Hospital in Finland. From 2015 to 2016, he was a Research Scholar with the Department of Electrical Engineering, IIT Delhi, India.

Dr. Dwivedi has received several awards such as the Certificate of Academic Excellence and the Certificate of Merit for his top academic performances; and scholarships, including the Imperial College President's PhD Scholarship and the GATE Scholarship from All India Council for Technical Education (AICTE), Government of India, for academic years 2013-2015. He has contributed to 33 peer-reviewed research papers in journals and international conferences, and 4 book chapters. His research interests include biomedical signal processing, machine learning algorithms and ultra-low power wearable systems for long-term continuous monitoring of physiological. Dr. Dwivedi received the "Best Paper Award" for his work at the CCPSAT 2022 conference. Dr. Dwivedi is a Fellow of the Higher Education Academy, UK; and a Member of IEEE and IET.

Manisha Guduri (S'14-M'18-SM'22) received her Ph.D. degree in Electronics and Communications Engineering from Birla Institute of Technology, Mesra (Deemed University), Ranchi, India in July 2018. She received her PG Diploma in Cyber laws and Intellectual Property Rights from University of Hyderabad in 2022.

She is currently a post-doctoral fellow at the University of Louisiana at Lafayette, USA. She worked as Associate Professor & Dean R&D in KG Reddy College of Engineering & Technology, Hyderabad and Institute of Aeronautical Engineering, Hyderabad, India.

She is the author or co-author of 45+ research papers in reputed journals (IEEE Transactions, Springer, Elsevier, JSTS, etc), book chapters and international conferences. Her research interests include Artificial Intelligence, smart healthcare, and VLSI/CAD design for CMOS technologies, ultralow-power nanoscale circuits for portable/wearable/energy-harvesting applications.

Aminul Islam is a Senior Member of IEEE since 2015, and corporate member of Institute of Engineers (India). Until November 2006, he was with Indian Air Force. Since November 2006, he has been in the Department of ECE, Birla Institute of Technology, where he is currently an Associate Professor.

His broad research area is VLSI, Microelectronics, nanoelectronics and spintronics covering a wide spectrum of memory, digital, analog and RF and mixed-signal circuit design. Research interests include VLSI Design/CAD for nanoscale silicon and non-silicon technologies which center around the emerging nanoelectronics and spintronics devices and circuits like, SiC U-MOSFET, SiC V-MOSFET, VDMOSFET, FinFET, CNFET, HEMT, SRAM, MRAM, RRAM, PCRAM, power- and variability-aware design, RF device modeling and circuit design, design of ultralow-power nanoscale circuits for portable/ wearable/ energy-harvesting applications. He has authored/ coauthored more than 301 publications in refereed journals (116), conferences (139), chapters in Springer/Elsevier book (46) and 4 Indian Patents including 19 research papers in IEEE transactions.

He has supervised/supervising 60 UG students, 18 PG students and 09 PhD scholars. He was granted a research project titled "Study of HEMT and its performance in amplifier circuit" of worth Rs. 23.742 lakhs by DRDO, Govt. of India. He is a reviewer of various international journals such as IEEE Transactions on Circuits and Systems I: Regular Papers, IEEE Transactions on Device and Materials Reliability, IEEE Transactions on Magnetics. IEEE Transactions on VLSI Systems, IEEE Access, etc.

This work is licensed under a Creative Commons Attribution 4.0 License. For more information, see https://creativecommons.org/licenses/by/4.0/